

A Hybrid MPI-OpenMP Parallel Implementation for Simulating Taylor-Couette Flow

Liang Shi^{a,b,1,*}, Markus Rampp^c, Björn Hof^{a,d}, Marc Avila^e

^a*Max Planck Institute for Dynamics and Self-Organization (MPIDS), 37077 Göttingen, Germany*

^b*Institute of Geophysics, University of Göttingen, 37077 Göttingen, Germany*

^c*Computing Centre (RZG) of the Max Planck Society and the Max-Planck-Institute for Plasmaphysics, Boltzmannstr. 1, 85748 Garching, Germany*

^d*IST Austria, 3400 Klosterneuburg, Austria*

^e*Institute of Fluid Mechanics, Friedrich-Alexander-Universität Erlangen-Nürnberg, 91058 Erlangen, Germany*

Abstract

A hybrid-parallel direct-numerical-simulation method for turbulent Taylor-Couette flow is presented. The Navier-Stokes equations are discretized in cylindrical coordinates with the spectral Fourier-Galerkin method in the axial and azimuthal directions, and high-order finite differences in the radial direction. Time is advanced by a second-order, semi-implicit projection scheme, which requires the solution of five Helmholtz/Poisson equations, avoids staggered grids and renders very small slip velocities. Nonlinear terms are computed with the pseudospectral method. The code is parallelized using a hybrid MPI-OpenMP strategy, which is simpler to implement, reduces inter-node communications and is more efficient compared to a flat MPI parallelization. A strong scaling study shows that the hybrid code maintains very good scalability up to $\mathcal{O}(10^4)$ processor cores and thus allows to perform simulations at higher resolutions than previously feasible, and opens up the possibility to simulate turbulent Taylor-Couette flows at Reynolds numbers up to $\mathcal{O}(10^5)$. This enables to probe hydrodynamic turbulence in Keplerian flows in experimentally relevant regimes.

*Corresponding author

Email addresses: liang.shi@ds.mpg.de (Liang Shi), markus.rampp@rzg.mpg.de (Markus Rampp), bhof@ist.ac.at (Björn Hof), marc.avila@fau.de (Marc Avila)

¹Present address (visiting scientist): IST Austria, 3400 Klosterneuburg, Austria.

Keywords: direct numerical simulation, Taylor-Couette flow, hybrid parallelization, pseudospectral method, finite difference

1. Introduction

Rotating fluid flows with radially increasing angular momentum are known to be linearly stable because of the inviscid Rayleigh criterion [1]. A particularly important application is astrophysical Keplerian flow, with angular velocity profile decreasing radially as $\Omega \propto r^{-3/2}$. Whether Keplerian flows become turbulent because of nonlinear instabilities or remain laminar even at extreme Reynolds numbers, has great implications for accretion processes in weakly-ionized astrophysical disks [2]. This question has been recently investigated with experiments of fluid flows between rotating cylinders (Taylor-Couette flow, TCf), which can in principle approximate Keplerian profiles. Experiments conducted by Ji *et al.* [3, 4] found no hydrodynamic turbulence in quasi-Keplerian TCf in the range $Re \sim \mathcal{O}(10^5 - 10^6)$, whereas similar studies [5, 6] report strongly turbulent flows that could account for the observed accretion rates in astrophysical disks. This discrepancy may arise from the axial boundary conditions: numerical simulations of the experimental setups show that top and bottom endwalls confining the fluid strongly disrupt Keplerian velocity profiles and causes turbulence to arise already at $Re \sim \mathcal{O}(10^3)$ [7]. Hence, the interpretation and extrapolation of experimental data remains controversial because of the prominent role played by axial endwalls.

Numerical simulations with axially periodic boundaries resolve this problem and allow to directly probe the stability of Keplerian flows. However, this requires achieving very high Reynolds numbers $Re \sim \mathcal{O}(10^5)$. Moreover, as the key question is concerned about the existence of turbulence, modeling strategies such as Reynolds-averaged equations (RANS) and Large-Eddy Simulation (LES) are precluded and one has to resort to direct numerical simulation (DNS) of the Navier-Stokes equations (see [8] for details about these simulation techniques). Starting with the study of homogeneous isotropic turbulence conducted by Orszag and Patterson [9], DNS has been proven as a very powerful approach to explore the physics of turbulent flows (see Ref. [10], [11]). It has been widely used in fundamental research on both transitional and fully-developed turbulence in boundary layers over a flat plate (e.g. [12], [13]), channel (e.g. [14], [15]), pipe (e.g. [16], [17]) and Couette flows (e.g. [18], [19]). Distinguished from RANS and LES, a carefully

performed DNS resolves all temporal and spatial scales relevant to turbulence and thus provides data of high fidelity. Its advantage is also its main drawback: resolving the physics of turbulence implies a scaling of the computational complexity as $\mathcal{O}(Re^3)$ [8].

In this paper we develop a highly efficient DNS code for TCf with axially periodic boundary conditions using a hybrid two-level parallelization strategy. It enables DNS to be performed up to $Re \sim \mathcal{O}(10^5)$, and thus provides access to a broad range in the parameter space of TCf, including quasi-Keplerian flows at experimentally relevant Reynolds numbers. The most efficient method for discretizing partial differential equations with periodic boundary conditions is the spectral Fourier–Galerkin method, so we use this in the axial and azimuthal directions. Many authors use the spectral Galerkin-method in the non-periodic radial direction by employing Chebyshev, Legendre or Jacobi polynomials. The two latter render however a computational complexity of $\mathcal{O}(M^2)$, where M is the degree of the approximation, due to the lack of fast transformations between physical and spectral spaces. This makes computations too expensive at large Reynolds number. In contrast, with the Chebyshev method the fast cosine transform allows it to keep the cost at $\mathcal{O}(M \log(M))$. However, in order to use accurate quadratures the projection basis must be different from the basis used to discretize the Navier-Stokes equations (Petrov-Galerkin method) [20, 21]. On the other hand, if the spectral method is used directly at a collocation grid (in physical space) the resulting differentiation matrices are dense. Hence the solution of the Poisson equations, for example with the diagonalization method [22], requires $\mathcal{O}(M^2)$ operations. A common drawback of all the aforementioned spectral methods is that the density of collocation nodes towards the boundaries scales as $\mathcal{O}(M^2)$. Although this allows to properly resolve boundary layers with relatively low resolutions, at large Reynolds numbers the clustering is excessive and the required resolution is often given by the spacing of nodes far from the boundaries. Moreover, this clustering poses a severe restriction on the time step of $\Delta t = \mathcal{O}(M^{-2})$ because of the CFL condition. Although transformations of the node distribution have been proposed [23], these result in the loss of the spectral convergence. Finally, it becomes impractical to use the Chebyshev method for large resolutions $M \gtrsim 600$, as needed in the simulation of turbulence at large Re (see §5). For these reasons we use the high-order finite-difference (FD) method in the radial direction, which makes the stretching of grid nodes straightforward.

The dimensionless, incompressible Navier-Stokes equations in primitive

variables are integrated in time with a second-order $\mathcal{O}(\Delta t^2)$ time-splitting scheme proposed by Hugues & Randriamampianina [24]. The scheme is semi-implicit and is second-order accurate also for the pressure, rendering a very small $\mathcal{O}(\Delta t^3)$ slip-velocity error at the boundary while fulfilling the incompressibility constraint. It is straightforward to implement: it avoids staggered grids and requires the solution of five equations of Poisson or Helmholtz type. The nonlinear advective term is computed in physical space with the pseudospectral method. The code is parallelized by combining the Message Passing Interface (MPI) and the Open Multiprocessing (OpenMP) paradigms. The Fourier-Galerkin method leads to mode-decoupled linear equations, which makes the one-dimensional MPI parallelization rather straightforward to implement. OpenMP threading within MPI tasks allows to efficiently use modern high performance computing (HPC) architectures and mitigates the overhead induced by MPI All-to-all inter-task communications which are typical of spectral methods.

The paper is structured as follows. In §2, we formulate the Taylor–Couette problem and then present the numerical method in §3. In §4 we describe the parallelization strategy employed in the code and its implementation. The accuracy and performance of the code are discussed in §5 and §6, respectively, before the conclusions in §7.

2. Governing Equations and Geometry

We solve the equations governing the motion of an incompressible fluid of kinematic viscosity ν and constant density ρ

$$\partial_t \mathbf{u} + \mathbf{u} \cdot \nabla \mathbf{u} = -\frac{1}{\rho} \nabla p^h + \nu \Delta \mathbf{u}, \quad \nabla \cdot \mathbf{u} = 0, \quad (1)$$

where $\mathbf{u}(\mathbf{r}, t)$ is the velocity field and $p^h(\mathbf{r}, t)$ is the hydrodynamic pressure. Here cylindrical coordinates $\mathbf{r} = (r, \theta, z)$ are used. The geometry of the system is shown in Fig. 1 and consists of fluid confined between two concentric cylinders. The inner (outer) cylinder has radius r_i (r_o) and rotates at a speed of Ω_i (Ω_o). The Reynolds number in the inner and outer cylinder is defined as $Re_{i,o} = \Omega_{i,o} r_{i,o} d / \nu$, where $d = r_o - r_i$ is the gap between the cylinders. The geometry is fully specified by two dimensionless parameters: the radii-ratio $\eta = r_i / r_o$ and the length-to-gap aspect-ratio $\Gamma = L_z / d$, where L_z is the axial length of the cylinders. At the cylinders no-slip boundary

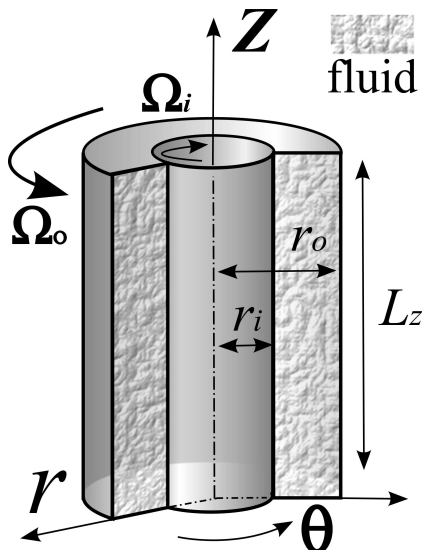


Figure 1: Schematic of the Taylor-Couette system in cylindrical coordinates. The inner and outer cylinder rotate independently with speeds Ω_i and Ω_o , respectively. No-slip boundary conditions at the cylinder are used together with axially periodic boundary conditions. The fluid between the cylinders (hatched region) moves by the shear force due to the fluid viscosity.

conditions are applied, whereas in the axial direction periodic boundary conditions are imposed to avoid endwall effects. This approximates the case of very long cylinders. In the azimuthal direction periodic boundary conditions occur naturally. However, it is often computationally convenient to simulate only an angular section $L_\theta \leq 2\pi$ of the cylinders, and periodic boundary conditions are then used for $\theta \in [0, L_\theta]$. This is justified provided that the correlation length of the turbulent flow in the azimuthal direction is shorter than $r_i L_\theta$ [19].

Henceforth, all variables will be rendered dimensionless using d , $\tau = d^2/\nu$, and ν^2/d^2 as units for space, time, and the reduced pressure $p = p^h/\rho$, respectively. The Navier-Stokes equations (1) for this scaling become

$$\begin{aligned} \partial_t \mathbf{u} + \mathbf{u} \cdot \nabla \mathbf{u} &= -\nabla p + \Delta \mathbf{u} \\ \nabla \cdot \mathbf{u} &= 0. \end{aligned} \tag{2}$$

In cylindrical coordinates the equations read

$$\begin{aligned}
(\partial_t + \mathbf{u} \cdot \nabla)u_r - u_\theta^2/r &= -\partial_r p + \Delta u_r - u_r/r^2 - 2\partial_\theta u_\theta/r^2 \\
(\partial_t + \mathbf{u} \cdot \nabla)u_\theta + u_\theta u_r/r &= -\partial_\theta p/r + \Delta u_\theta - u_\theta/r^2 + 2\partial_\theta u_r/r^2 \\
(\partial_t + \mathbf{u} \cdot \nabla)u_z &= -\partial_z p + \Delta u_z, \\
u_r/r + \partial_r u_r + \partial_\theta u_\theta/r + \partial_z u_z &= 0.
\end{aligned} \tag{3}$$

with $\nabla = (\partial_r, \partial_\theta/r, \partial_z)$ and $\Delta = \partial_r^2/r + \partial_{rr}^2 + \partial_{\theta\theta}^2/r^2 + \partial_{zz}^2$. Note that the Reynolds numbers enter the system through the boundary conditions

$$\begin{aligned}
u_\theta(r_{i,o}, \theta, z) &= Re_{i,o}, \\
u_{r,z}(r_{i,o}, \theta, z) &= 0, \\
\mathbf{u}(r, \theta, z) &= \mathbf{u}(r, \theta + L_\theta, z), \\
\mathbf{u}(r, \theta, z) &= \mathbf{u}(r, \theta, z + \Gamma).
\end{aligned} \tag{4}$$

By taking the divergence of the first equation and then applying the incompressibility condition, we obtain a Poisson equation for the pressure,

$$\Delta p = -\nabla \cdot \mathbf{N}(\mathbf{u}), \quad \text{where} \quad \mathbf{N}(\mathbf{u}) = \mathbf{u} \cdot \nabla \mathbf{u}, \tag{5}$$

with consistent boundary conditions [25]

$$\partial_n p|_{r=r_{i,o}} = \mathbf{n} \cdot [-\partial_t \mathbf{u} - \mathbf{N}(\mathbf{u}) + \Delta \mathbf{u}]. \tag{6}$$

As explained in §3.2, this equation will be solved for the pressure prediction.

3. Numerical Formulation

The governing equations (3) are solved for the primitive variables (\mathbf{u}, p) . We discretize the equations with a combination of the spectral-Fourier method with the finite-difference method (FD) in space, whereas time is advanced with a semi-implicit fractional-step method proposed by Hugues and Ramiandrianampianina [24], who employ a second-order-accurate backward-differentiation formula with second-order extrapolation for the nonlinear term. The pseudospectral technique with 3/2-dealiasing [9] is applied to compute the nonlinear term $\mathbf{N}(\mathbf{u})$ in physical space.

3.1. Spatial discretization

In the periodic axial and azimuthal directions, the velocity field and pressure are approximated as

$$\begin{aligned}\mathbf{u}(r, \theta, z) &= \sum_{l=-L}^L \sum_{n=-N}^N \hat{\mathbf{u}}^{ln}(r) e^{i(lk_z z + nk_\theta \theta)}, \\ p(r, \theta, z) &= \sum_{l=-L}^L \sum_{n=-N}^N \hat{p}^{ln}(r) e^{i(lk_z z + nk_\theta \theta)},\end{aligned}\tag{7}$$

where k_z is the minimum (fundamental) axial wavenumber and fixes the axial non-dimensional length $\Gamma = 2\pi/k_z$ of the computational domain. Similarly, $L_\theta = 2\pi/k_\theta$ is the azimuthal length; $k_\theta = 1$ corresponds to the natural periodic boundary condition in the azimuthal direction, whereas $k_\theta = 4$ corresponds to one quarter of an annulus. The hat symbol $\hat{\cdot}$ in (7) denotes quantities in Fourier space and the tuple (L, N) determines the spectral numerical resolution.

By substituting (7) into (3) and projecting the result onto a basis $e^{-i(lk_z z + nk_\theta \theta)}|_{l=-L, n=-N}^{L, N}$, we obtain the mode-decoupled Navier-Stokes equations. For each Fourier mode (l, n) , they read

$$\begin{aligned}\partial_t \hat{u}_r + \hat{N}_r &= -\partial_r \hat{p} + \hat{\Delta} \hat{u}_r - \hat{u}_r/r^2 - 2ink_\theta \hat{u}_\theta/r^2, \\ \partial_t \hat{u}_\theta + \hat{N}_\theta &= -ink_\theta \hat{p}/r + \hat{\Delta} \hat{u}_\theta - \hat{u}_\theta/r^2 - 2ink_\theta \hat{u}_r/r^2, \\ \partial_t \hat{u}_z + \hat{N}_z &= -ilk_z \hat{p} + \hat{\Delta} \hat{u}_z.\end{aligned}\tag{8}$$

Here $\hat{\Delta} = \partial_r/r + \partial_{rr} - n^2 k_\theta^2/r^2 - l^2 k_z^2$, and the superscripts (l, n) have been omitted for clarity. Note that the nonlinear term couples Fourier modes and it is thus computed in physical space with the pseudospectral method. Details of the implementation and parallelization of the nonlinear term are given in §4. Equations (8) couple the radial and azimuthal velocities. By applying the following change of variables [26]

$$\begin{aligned}\hat{u}_+ &= \hat{u}_r + i\hat{u}_\theta, \\ \hat{u}_- &= \hat{u}_r - i\hat{u}_\theta,\end{aligned}$$

to equation (8), we yield the decoupled equations

$$\begin{aligned}\partial_t \hat{u}_+(r) + \hat{N}_+(r) &= -\partial_r \hat{p}(r) + nk_\theta \hat{p}(r)/r + (\hat{\Delta} - 1/r^2 - 2nk_\theta/r^2) \hat{u}_+, \\ \partial_t \hat{u}_-(r) + \hat{N}_-(r) &= -\partial_r \hat{p}(r) - nk_\theta \hat{p}(r)/r + (\hat{\Delta} - 1/r^2 + 2nk_\theta/r^2) \hat{u}_-, \\ \partial_t \hat{u}_z(r) + \hat{N}_z(r) &= -ilk_z \hat{p}(r) + \hat{\Delta} \hat{u}_z,\end{aligned}\tag{9}$$

where $\hat{N}_\pm = \hat{N}_r \pm i\hat{N}_\theta$.

We use a standard high-order, central finite-difference method to approximate the radial derivatives in equations (9) (see Ref. [27]). The radial nodes are distributed as [23]

$$r_j = \frac{1 + \eta}{2(1 - \eta)} + \frac{\sin^{-1}(-\alpha \cos(\pi j/M))}{2 \sin^{-1} \alpha}, \quad j = 0, \dots, M. \quad (10)$$

For $\alpha = 1$ the grid is uniform, whereas for $\alpha \rightarrow 0$ the Chebyshev collocation points are obtained. Here stencils of $n_s = 9$ points, corresponding to a scheme of formally order 7 was found to give the best compromise in our tests. Note that we reduce the stencil length gradually towards the boundaries in order to keep the FD-matrices banded. We show in §5 that due to the clustering of nodes near the walls with typical values of $\alpha = 0.5$ this reduction of the order of accuracy does not produce a larger error at the boundaries.

With (L, N) Fourier modes and M radial nodes, the number of grid points in physical space is $(n_r, n_\theta, n_z) = (M, 2N + 1, 2L + 1)$ in radial, azimuthal and axial direction, respectively. Note that we dealias the nonlinear term by computing it on a grid of $(M, 3N + 1, 3L + 1)$ points.

3.2. Temporal scheme

A stiffly stable temporal scheme based on a backward differentiation formula with extrapolation for the nonlinear term is adopted (see Ref. [24, 28]). It reads

$$\frac{3\mathbf{u}^{i+1} - 4\mathbf{u}^i + \mathbf{u}^{i-1}}{2\Delta t} + 2\mathbf{N}^i(\mathbf{u}) - \mathbf{N}^{i-1}(\mathbf{u}) = -\nabla p^{i+1} + \Delta \mathbf{u}^{i+1}. \quad (11)$$

In the literature this is often referred to as Adams-Bashforth backward-difference method of second order (AB2BD2). The viscous terms are discretized implicitly in time, whereas the nonlinear terms are treated explicitly in time. At each time step, equation (11) is solved through a fractional step method proposed by Hugues and Randriamampianina [24]. The method is summarized below. Here $(\hat{\mathbf{u}}^i, \hat{p}^i)$ denote the spectral coefficients at the i^{th} time step.

- 1) Obtain spectral coefficients of the nonlinear term, $\hat{\mathbf{N}}^i(\mathbf{u})$, using the 3/2-dealiasing rule
 - Do matrix-vector multiplication to calculate $\partial_r \hat{\mathbf{u}}^i$ (FD method)

- Compute dot product in Fourier space to calculate $\partial_\theta \hat{\mathbf{u}}^i$ and $\partial_z \hat{\mathbf{u}}^i$
- Perform Fourier transform of $\partial_{r,\theta,z} \hat{\mathbf{u}}^i$ and $\hat{\mathbf{u}}^i$ to obtain the velocity field and all its derivatives in physical space;
- Calculate $\mathbf{N}^i(\mathbf{u}) = \mathbf{u}^i \cdot \nabla \mathbf{u}^i$;
- Perform inverse Fourier transform to obtain the spectral coefficients $\hat{\mathbf{N}}^i(\mathbf{u})$.

2) Obtain the pressure prediction, \hat{p}^* : solve the Poisson equation

$$\Delta \hat{p}^* = \nabla \cdot [-2\hat{\mathbf{N}}^i(\mathbf{u}) + \hat{\mathbf{N}}^{i-1}(\mathbf{u})], \quad (12)$$

with consistent Neumann boundary conditions (6).

3) Obtain the velocity prediction, $\hat{\mathbf{u}}^*$: solve the three Helmholtz equations

$$\frac{3\hat{\mathbf{u}}^* - 4\hat{\mathbf{u}}^i + \hat{\mathbf{u}}^{i-1}}{2\Delta t} + 2\hat{\mathbf{N}}^i(\mathbf{u}) - \hat{\mathbf{N}}^{i-1}(\mathbf{u}) = -\nabla \hat{p}^* + \Delta \hat{\mathbf{u}}^* \quad (13)$$

with Dirichlet boundary conditions (4).

4) Correct via an intermediate variable $\phi = \frac{2\Delta t(\hat{p}^{i+1} - \hat{p}^*)}{3}$: The incompressibility condition $\nabla \cdot \hat{\mathbf{u}}^{i+1} = 0$ leads to a Poisson equation for ϕ with homogeneous Neumann boundary conditions (see Ref. [25, 24])

$$\begin{aligned} \Delta \phi &= \nabla \cdot \hat{\mathbf{u}}^*, \\ \partial_r \phi|_{r=r_{i,o}} &= 0 \end{aligned} \quad (14)$$

5) Compute pressure and velocity correction, \hat{p}^{i+1} and $\hat{\mathbf{u}}^{i+1}$:

$$\begin{aligned} \hat{p}^{i+1} &= \hat{p}^* + 3\phi/(2\Delta t) \\ \hat{\mathbf{u}}^{i+1} &= \hat{\mathbf{u}}^* - \nabla \phi \end{aligned} \quad (15)$$

6) Go back to step 1

The Navier-Stokes equations are thus advanced in time by solving five systems of linear equations (12)-(14), of Poisson or Helmholtz type. This method accounts for a divergence-free velocity field and a small slip at the wall of the order of $\mathcal{O}(\Delta t^3)$ in the tangential velocities, u_z and u_θ . We note that the method was originally developed and tested [24] for the two-dimensional Navier-Stokes equation discretized on a Chebyshev-Chebyshev

collocation grid, and the Poisson and Helmholtz equations were solved using the double diagonalization method. Here, the FD-discretized Poisson and Helmholtz equations render banded matrices which are solved with the LU-method. The decompositions are precomputed at the beginning of a simulation and at each time step only backward and forward substitutions need to be computed, resulting in an operation count of $\mathcal{O}(M)$ for the solution of each system. Note that for the axially and azimuthally invariant Fourier mode, $n = l = 0$, the Poisson equations (12) and (14) are singular: their solution is defined up to a constant because of the Neumann boundary conditions. Here a Dirichlet homogeneous boundary condition was employed at the outer cylinder to select a particular solution.

4. Parallelization scheme and its implementation

A hybrid MPI-OpenMP parallelization strategy is adopted for the implementation of the code. Since the linear equations (12)–(14) are mode-independent, it is convenient to employ an MPI-based, one-dimensional domain decomposition (also known as “slab” decomposition, Fig. 2): The Fourier coefficients $(\hat{u}_+, \hat{u}_-, \hat{u}_z, \hat{p})$ corresponding to different modes are distributed across the MPI tasks which allows to solve equations (12)–(14) concurrently, without any inter-task communication. Each of the N_{tasks} MPI tasks operates on data corresponding to a number of $m_\theta \cdot m_z / N_{\text{tasks}}$ modes, where $(m_r, m_\theta, m_z) = (M, N + 1, 2L)$ are the dimensions of variables in Fourier space. OpenMP threading inside each MPI task allows to efficiently exploit the remaining coarse-grained parallelism (see below).

We compute the nonlinear term (step 1 in Section 3.2) by performing global matrix transpositions (Fig. 2) of the discretized fields $\partial_r \hat{\mathbf{u}}$ and $\hat{\mathbf{u}}$ such that for each radial point the complete spectrum of Fourier modes is localized in one MPI task. This requires a collective communication operation of type “all-to-all” but allows to most efficiently compute the Fourier transformations and the derivatives with respect to the spectral coordinates, namely θ and z . Finally, inverse transpositions are performed for the resulting array $\hat{\mathbf{N}}$.

In our applications, typically $m_\theta \cdot m_z \gg m_r$ applies, i.e. there are much more Fourier modes than radial grid points. Hence, the number of MPI tasks in our slab decomposition is bounded by $N_{\text{tasks}} \leq m_r$ (cf. Fig. 2) and consequently the maximum achievable parallel speedup would be limited by m_r . However, OpenMP threads allow to parallelize over the $m_\theta \cdot m_z / N_{\text{tasks}}$ modes within a MPI task while retaining the one-dimensional MPI domain decom-

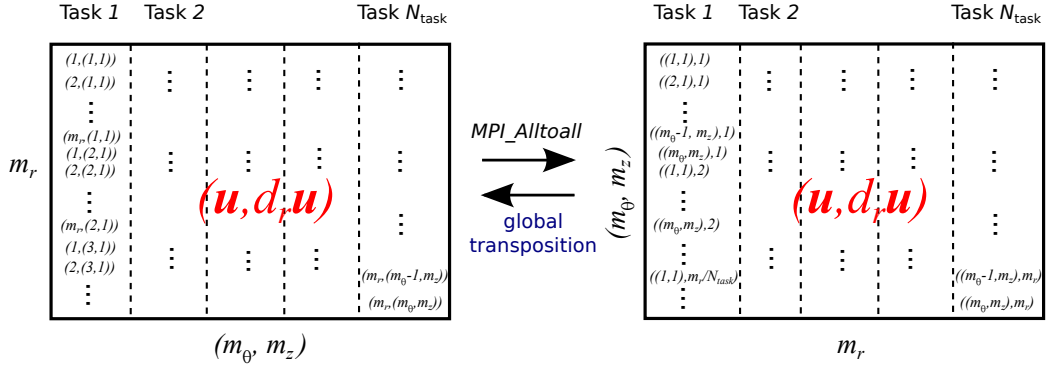


Figure 2: Schematic of the MPI-based, one-dimensional “slab” domain decomposition and the global transposition by using the function `MPI_Alltoall()`. Mode-independent spectral coefficients in Fourier space are distributed among different MPI tasks. Each variable has a dimension of (m_r, m_θ, m_z) .

position which is conceptually straightforward to implement. Similarly, we can exploit concurrency in the nonlinear part if $N_{\text{tasks}} < m_r$ applies. In addition, the Fourier transformations and the individual partial derivatives required for evaluating $\mathbf{u} \cdot \nabla \mathbf{u}$ are computed concurrently and the transposition of $\partial_r \hat{\mathbf{u}}$ is overlapped with the computation of \mathbf{u} , $\partial_\theta \mathbf{u}$, and $\partial_z \mathbf{u}$.

Theoretically, this strategy allows to utilize a number of $\min(m_r, m_\theta \cdot m_z) \cdot N_{\text{threads}}$ processor cores where N_{threads} is the maximum number of threads a shared-memory compute node provides. Current high performance computing (HPC) platforms feature at least 16 cores with up to 32 logical threads per node (e.g. Intel Sandy-Bridge E5 clusters), and thread-based concurrency on the node-level is expected to increase substantially in the near future, in particular with the upcoming many-core processors and GPU-accelerated nodes [29]. In practice, we achieve excellent parallel efficiencies when MPI tasks are mapped to the individual “sockets” (i.e. CPUs or NUMA domains) of a compute node and the number of OpenMP threads equals the number of physical cores per socket. Due to the smaller number of MPI tasks per node (compared with a plain MPI parallelization) the amount of inter-node communications is reduced in the global transposition. This transposition, which is implemented by `MPI_Alltoall` collective communication and task-local transpositions, ultimately limits the overall parallel scalability of the code at high task counts (see Section 6).

The code is implemented in FORTRAN 90 and has been ported to a number of major HPC architectures, including IBM Power and BlueGene, as

well as compute clusters based on x86_64 processors and high-performance interconnects such as InfiniBand. We employ vendor-optimized BLAS and LAPACK routines for the matrix-vector multiplication (BLAS level-2 routine DGEMV) and the linear solvers (variants of LAPACK routines DGBTRF, DGBTRS taken e.g. from the Intel Math Kernel Library, or IBM ESSL), respectively, and utilize the FFTW library [30] for performing the Fourier transformations in the nonlinear part of the code. For data output we employ the parallel HDF5 libraries which enable collective output of the MPI-distributed data into a single file in a transparent and efficient way. This facilitates data handling, post-processing and visualization, *e.g.* with VisIT or Paraview (cf. Fig. 9).

5. Numerical Accuracy and Code Validation

The code has been tested over a wide range of Reynolds numbers $Re \in [50, 100\,000]$. A number of specific test cases will be given in the following.

5.1. Laminar flow

We firstly computed the laminar velocity profile, which is also known as circular Couette flow. It can be expressed as $\mathbf{U} = (0, U_\theta(r), 0)$, where $U_\theta(r) = C_1 r + C_2/r$ with $C_1 = (Re_o - \eta Re_i)/(1 + \eta)$ and $C_2 = \eta(Re_i - \eta Re_o)/((1 - \eta)(1 - \eta^2))$, corresponding to pure rotary shear flow. The tests were performed at $Re_i = 50$, $Re_o = 200$ and at $\eta = 0.5$. A non-uniform grid according to formula (10) is used in the radial direction, clustering at the boundaries. Fig. 3(left) shows the numerical velocity and pressure profiles for $\alpha \rightarrow 0$ (Chebyshev points) and $n_r = 32$, which match well with the theoretical curves (dashed lines). The distributions of the relative error $\epsilon_u(r) = |\frac{u_\theta - U_\theta}{U_\theta}|$ along the radial direction are shown in Fig. 3(right) for different stencil lengths n_s . The error is quite smoothly distributed at the bulk flow. As n_s is increased, the relative error decreases until approaching the machine precision. In order to make the best compromise between the computing time and the accuracy, $n_s = 9$ is chosen for the following tests.

To measure the global error, we integrate the local error ϵ_u over the radial direction, $\mathcal{E}_u = \int_{r_i}^{r_o} \epsilon_u r dr$, which is plotted in Fig. 4 as a function of n_r and the parameter α . In the left figure, \mathcal{E}_u scales as a power law with n_r for both $\alpha = 0$ and $\alpha = 0.5$. The power exponent is fitted to be about -11 , which is even better than as is expected from the 9-points-stencil FD scheme. The right figure shows that the error is minimized for $\alpha \simeq 0.5$ and that below 0.5

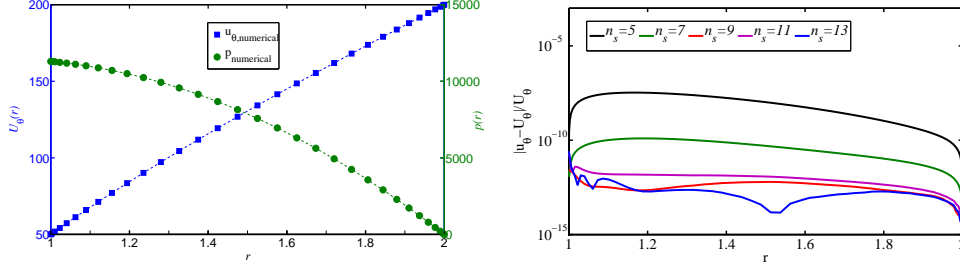


Figure 3: Laminar Couette flow. Left: The numerical and theoretical (dashed lines) streamwise velocity profile (blue squares) and pressure field (green circles). Right: The local relative error ϵ_u as a function of r . Here in the right figure $\Gamma = 2$ and $k_\theta = 2$, with a resolution of $(n_r, n_\theta, n_z) = (64, 8, 8)$. In the radial direction Chebyshev points are used, $\alpha \rightarrow 0$.

the errors are almost at the same level and thus are all acceptable at this Re . Except for n_r , which is varied in the left figure, the same resolution as in the above Fig. 3 was used.

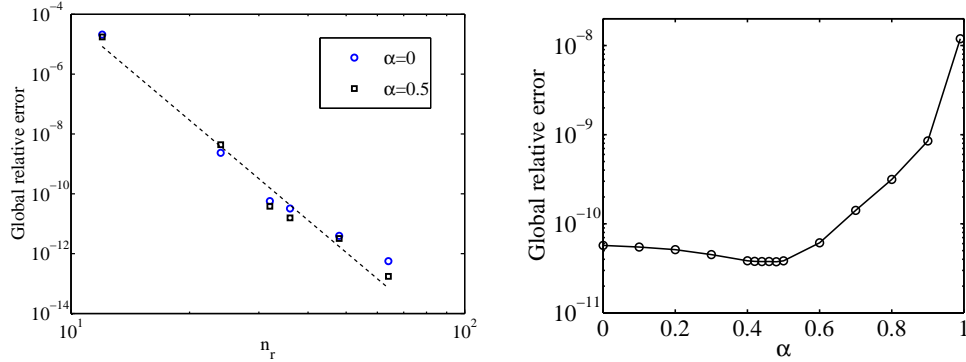


Figure 4: The global relative error \mathcal{E}_u as a function of (left) n_r and (right) α . The dashed line in the left figure is the power fit with an exponent about -11. The stencil length is $n_s = 9$. The resolution is $(n_r, n_\theta, n_z) = (32, 8, 8)$, except for n_r which is varied in the left figure.

5.2. Time-dependent flow and slip velocity at walls

Time-dependent periodic flow was computed at $Re_i = 458.1$, $Re_o = 0$, $\eta = 0.868$. The axial length was chosen as $\Gamma = 2\pi/k_z = 2.4$ and $k_\theta = 6$ to compare to the experimental observations of King *et al.* [31] and numerical simulations

of Marcus [22]. At these parameter values the flow is characterized by wavy Taylor vortices with azimuthal wavenumber 6, as shown in Fig. 5. Wavy Taylor vortices are a relative equilibrium: they consist of a constant pattern rotating as a solid at a constant wave speed. Marcus [22] notes: ‘*A test that is more sensitive than the comparison of torques is the comparison of the numerically computed wave speed with the experimentally observed wave speed*’. We performed this test with spatial resolution $(n_r, n_\theta, n_z) = 32 \times 32 \times 32$ and time-step size $\Delta t = 2 \times 10^{-5}$. The wave speed normalized by the rotation speed of the inner cylinder was accurately computed with a rigorous method based on Brent’s minimization algorithm [32]. Our result, namely a wave speed of $c = 0.34432$, with the pattern rotating at about one-third of the speed of the inner cylinder, agrees to all decimal places given in [31]. The same result was reproduced at higher resolutions and on various HPC platforms.

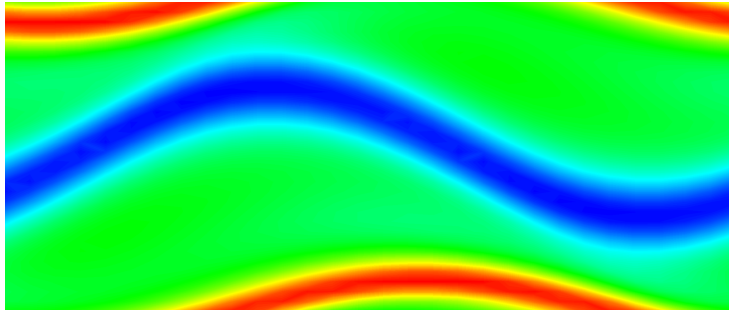


Figure 5: Contour plots of the streamwise velocity in the middle (θ, z) plane for wavy Taylor vortices. The outer cylinder is stationary, whereas the inner cylinder rotates with $Re_i = 458.1$. The geometrical parameters are $\eta = 0.868$ and $\Gamma = 2.4$ and only one sixth of the circle ($k_\theta = 6$) was used in the simulations and is displayed here.

We further examined the tangential velocity slip at the cylinders. In the projection scheme we employed, the incompressibility constraint $\nabla \cdot \mathbf{u} = 0$ is discretely fulfilled by construction, in that the Poisson equation for ϕ in §3.2 is derived by applying the divergence-free condition. However, the velocities at the inner and outer cylinders slip by an amount of $|\nabla\phi| = \mathcal{O}(\Delta t^3)$ after the correction step. We evaluated the L2-norm of the tangential velocity slip at the inner cylinder, $\int_\theta \int_z \sqrt{((u_\theta - Re_i)^2 - u_z^2)|_{r=r_i}} d\theta dz$. In Fig. 6 the relative velocity slip, i.e. slip velocity normalized with Re_i , is shown as a function of Δt for several radial resolutions n_r (see Fig. 6). For the lowest resolution

$n_r = 32$ the curve rapidly levels off, indicating that spatial-discretization errors dominate over temporal errors. Note that with the largest time-step size allowed for stability and lowest resolution we already obtain five digits in the accuracy of c . As n_r is increased the slip velocity decreases and its scaling gradually approaches a power law, here with an exponent of approximately 2.5. Improving the resolution in θ and z directions does not change the scaling and the reason why it deviates from the expected value of 3 is not clear. Nevertheless, we can conclude that in typical simulations the dominating source of error comes from the spatial discretization. The largest possible time-step size yields already very accurate results in the solution and very small slip velocities.

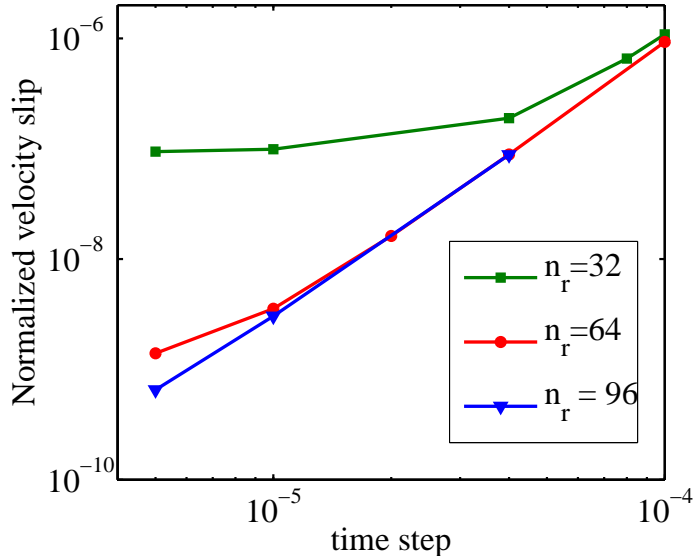


Figure 6: Normalized velocity slip at the inner cylinder against time-step size Δt for different n_r . The parameters are the same as in Figure 5. The spatial resolution in axial and azimuthal directions is $(n_\theta, n_z) = (32, 32)$

5.3. Localized turbulence at moderate Re

Localized turbulence, interspersed in the surrounding laminar flow, is a typical feature of transitional Reynolds numbers in shear flows. The turbulent stripe pattern found in the counter-rotating Taylor-Couette flow in the narrow-gap limit is an example. We obtained this pattern at $Re_i =$

680, $Re_o = -680$ with $\eta = 0.993$. The time-step size was $\Delta t = 2 \times 10^{-5}$ and the domain size in the axial and azimuthal directions was $\Gamma = 50$ and $r_o L_\theta = 5$. The θ -direction in our computational domain is tilted with an angle of 24° to the streamwise direction (for details see [33]). We tested the probability distributions of the splitting times of turbulent stripes reported in [33], which were obtained by using the spectral Petrov-Galerkin code of Meseguer *et al.* [21]. We here used $n_r = 32$ in the radial direction, whereas Shi *et al.* [33] used modified Chebyshev polynomials of degree up to 26. In both cases the azimuthal and axial resolutions are $n_\theta = 48$ and $n_z = 640$, respectively. The exponential distributions of splitting times obtained by both codes are statistically equivalent (see the inset in Fig. 7): our computed decay rate of the exponential distributions is well within the 95% confidence interval about the decay rate reported in [33].

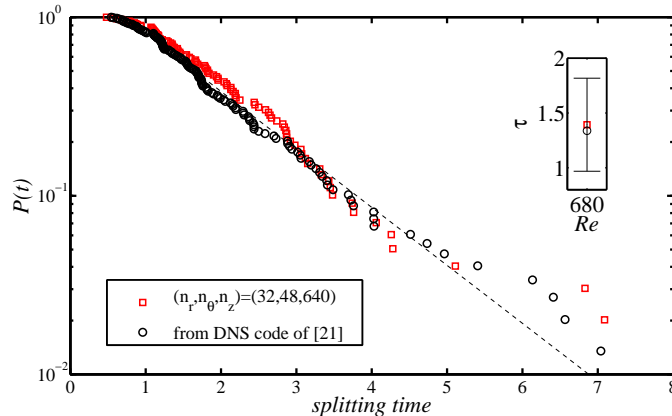


Figure 7: Probability distributions of the splitting time of single turbulent stripe at $Re_i = 680$, $Re_o = -680$ and at $\eta = 0.993$. The black data set was obtained with the spectral Petrov-Galerkin code of Meseguer *et al.* [21] and the red one with the new code with $n_r = 32$. In both cases the azimuthal and axial resolutions are $n_\theta = 48$ and $n_z = 640$, respectively. Inset: characteristic splitting time estimated by the sample mean, with the error bar corresponding the 95% confidential interval.

5.4. Turbulent flow at high Re

The robustness of the code was further validated at high Reynolds numbers in the linearly unstable regime, where the flow is fully turbulent. Here we computed the global torque exerted by the fluid on the inner and outer cylinders, which characterizes the turbulence intensity and the transport of

angular momentum [19]. The tests were done at $Re_i = 8000$ and stationary outer cylinder with $\eta = 0.5$, $\Gamma = 2\pi/k_z = \pi$ and $k_\theta = 2$. The time-step size is $\Delta t = 2 \times 10^{-7}$. As is shown in Fig. 8(top), the quasi-Nusselt number Nu_ω [19], which is the torque normalized by the torque of the laminar flow, converges to 8.815 at the resolution $(n_r, n_\theta, n_z) = (128, 192, 320)$. This value agrees very well to the value of 8.816 recently reported by Brauckmann and Eckhardt [19], who also used the spectral Petrov-Galerkin code of Meseguer *et al.* [21]. The temporal fluctuation of the Nusselt number obtained with the highest resolution is shown in the bottom figure. At this Re , we also examined the influence of the radial node distribution by varying the parameter α in Eq. 10. Three runs with $\alpha = 0, 0.5, 0.99$ were done, and all three render $Nu_\omega = 8.81 \pm 0.05$. The maximum time-step size is $\Delta t \approx 3 \times 10^{-7}$ in all cases and it is independent of α . This is explained by the fact that the CFL number is highest in the azimuthal direction. Thus at this Reynolds number the Chebyshev node distribution does not impose a restriction in the time-step, as one may have expected.

Another test run was performed at $Re_i = 10^5$, $Re_o = 79685$ and at $\eta = 0.71$. To the best of our knowledge, no DNS at such a high Re have been reported for Taylor-Couette flow. We used $k_\theta = 16$ and axial length $\Gamma = 0.5$, with a spatial resolution $(1152 \times 384 \times 384)$ and time step $\Delta t = 1 \times 10^{-9}$. The initial condition at $t = 0$ is taken from the optimal initial perturbation which gives the maximal transient energy growth [34] supplemented with very small three-dimensional noise. Fig. 9 shows the 3D contour plot of the streamwise vorticity, $\omega_\theta = \partial_z u_r - \partial_r u_z$, at $t = 5 \times 10^{-4}$ ($\simeq 3.3$ cylinder rotations) which illustrates a transiently turbulent flow state. The research is still ongoing and will be disseminated in future publications. We expect that the results will contribute to clarify the role of pure hydrodynamic turbulence, if any, in astrophysical discs [2].

6. Computational efficiency

6.1. Benchmark setup

In this section we report benchmark results obtained with the new code, using up to 8192 processor cores of an IBM iDataPlex compute cluster with Intel Sandy-Bridge processors and InfiniBand (FDR 14) interconnect. Each shared-memory compute node hosts two Intel Xeon E5-2670 eight-core processors (CPUs) with a clock frequency of 2.6 GHz. We employ Intel compilers

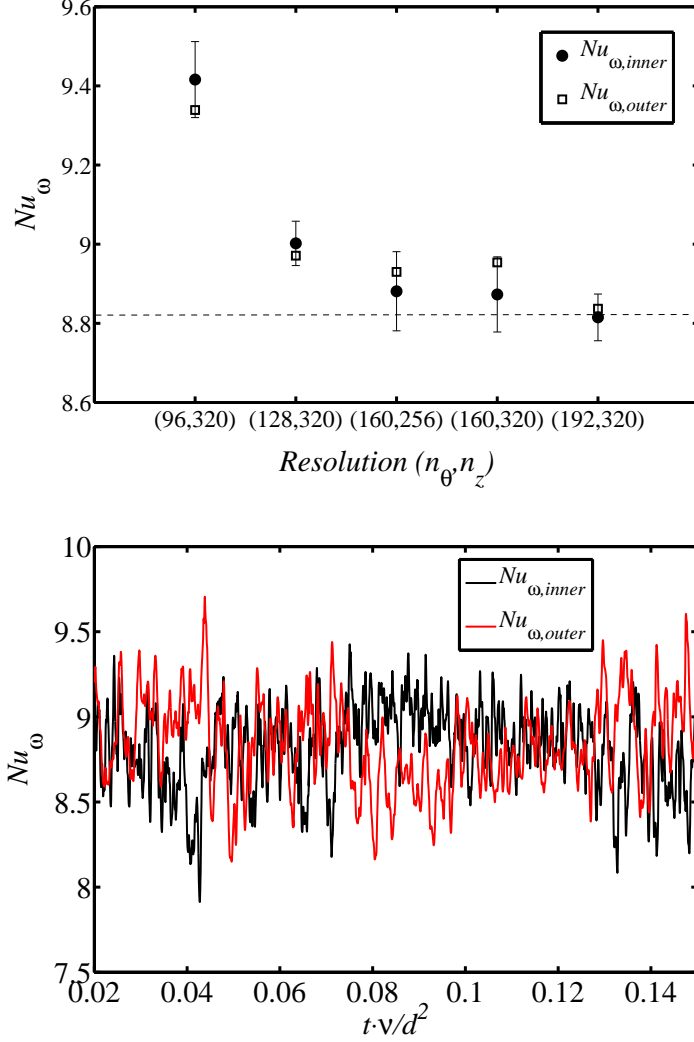


Figure 8: (Top) Quasi-Nusselt number at $Re_i = 8000$, $Re_o = 0$, $\eta = 0.50$, $\Gamma = 2\pi/k_z = \pi$ and $k_\theta = 2$, as a function of the azimuthal and axial resolutions for $n_r = 128$. The dashed line corresponds to the value ($Nu_\omega \simeq 8.816$) reported in [19]. The error bars indicate the 95% confidential interval. (Bottom) The temporal fluctuation of the quasi-Nusselt number at the highest resolution $(n_r, n_\theta, n_z) = (128, 192, 320)$.

(version 12.1), the Intel Math Kernel Library (MKL 10.3) and the FFTW library (version 3.3.2 with AVX kernels enabled).

We have performed two strong scaling studies, *i.e.*, the scaling of the

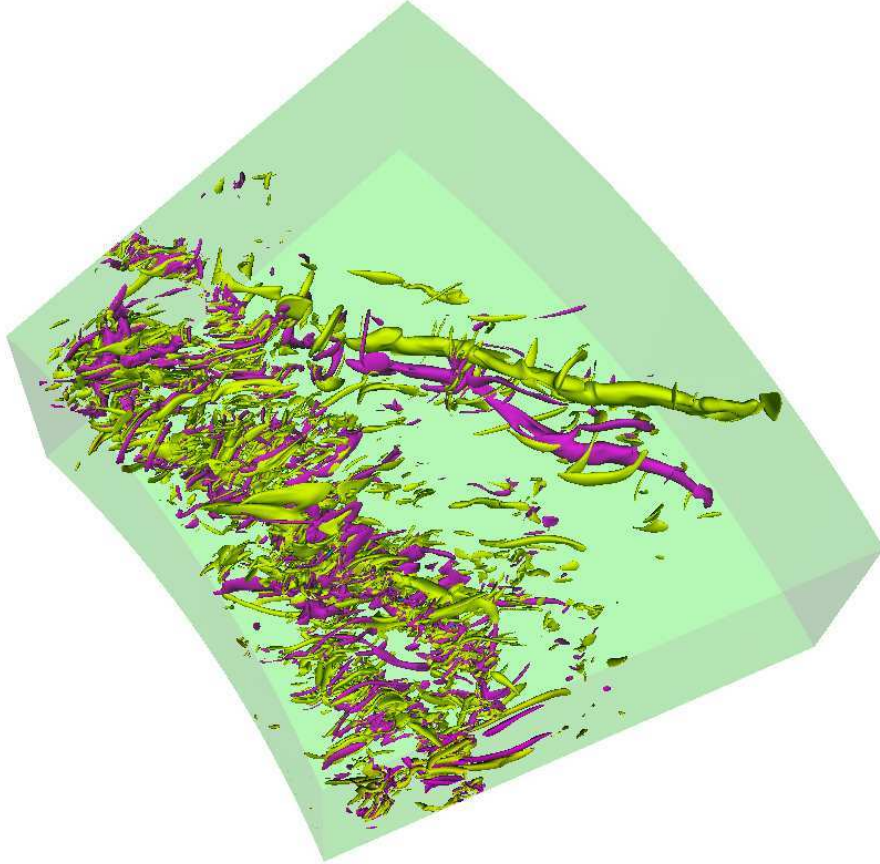


Figure 9: Isosurfaces of the streamwise vorticity in the quasi-Keplerian regime at $Re_i = 10^5$, $Re_o = 79685$, $\eta = 0.71$, $\Gamma = 0.5$ and $k_\theta = 16$. The resolution is $(n_r, n_\theta, n_z) = (1152, 384, 384)$.

runtime with the number of cores for a fixed problem size. Two different, representative setups were considered:

- a) a “SMALL” setup with number of grids points $(n_r, n_\theta, n_z) = (32, 384, 640)$. This setup is used to investigate the localized turbulence at the transitional stage ($Re \sim \mathcal{O}(10^2)$), where the structures inside the turbulence are relatively large. The probability distributions of the splitting time of localized turbulent stripe mentioned in Section 5 are obtained at this resolution level.
- b) a “LARGE” setup with number of grids points $(n_r, n_\theta, n_z) = (512, 256, 1024)$.

This resolution is representative of our ongoing studies of hydrodynamic turbulence in Taylor-Couette flows with quasi-Keplerian velocity profiles at Reynolds numbers up to $\mathcal{O}(10^5)$.

6.2. Benchmark results and discussion

Fig. 10 provides an overview of the strong scalability of the hybrid code. Different colors and symbols are used to distinguish runs which use different numbers of MPI tasks (N_{tasks}) and OpenMP threads (N_{threads}). The total number of processor cores is given by $N_{\text{cores}} = N_{\text{tasks}} \cdot N_{\text{threads}}$.

For both setups we observe good scalability up to the maximum number of cores our parallelization scheme admits on this compute platform, *i.e.*, $N_{\text{cores}} = 32 \cdot 16 = 512$ for the SMALL setup, and $N_{\text{cores}} = 512 \cdot 16 = 8192$ for the LARGE setup. Beyond a number of 8 threads per MPI task the scalability curves markedly level off. The code, however, still delivers a parallel efficiency of more than 0.5, which is commonly considered as the minimum for acceptable resource usage.

For the SMALL setup (Fig. 10, left) we show that up to a number of 8 threads per MPI task the run times for a given number of cores are virtually the same, independent of the distribution of the resources to MPI tasks and OpenMP threads (compare the green and the red symbols at $N_{\text{cores}} = 32$, or the red and the blue symbols at $N_{\text{cores}} = 128$). This indicates that the efficiency of our coarse-grained OpenMP parallelization is almost the same as the explicit, MPI-based domain decomposition, thus demonstrating the additional gain in flexibility of our hybrid approach compared to a plain MPI parallelization. Moreover, as the results for the LARGE setup (Fig. 10, right) show, it can even be more efficient to use less than the maximum of n_r MPI tasks for a given number of cores and utilize the resources with OpenMP threads (compare the green and the red symbols at moderate core counts). This is due to the fact that a lower number of MPI tasks per node reduces the amount of inter-node MPI communication (specifically the `MPI_Alltoall` communication pattern for the global transpositions) and hence network congestion. Notably, for the LARGE setup, the hybrid code shows nearly perfect linear scaling between 128 and 2048 cores and reaches a floating-point performance of about 16 GFlop/s per compute node which is roughly 5% of the nominal peak performance.

The details on the absolute run times and the parallel efficiencies of the whole code (the bottom row) as well as the individual parts of the algorithm (cf. Section 3.2) are listed in Table 1. The first column, which corresponds to a

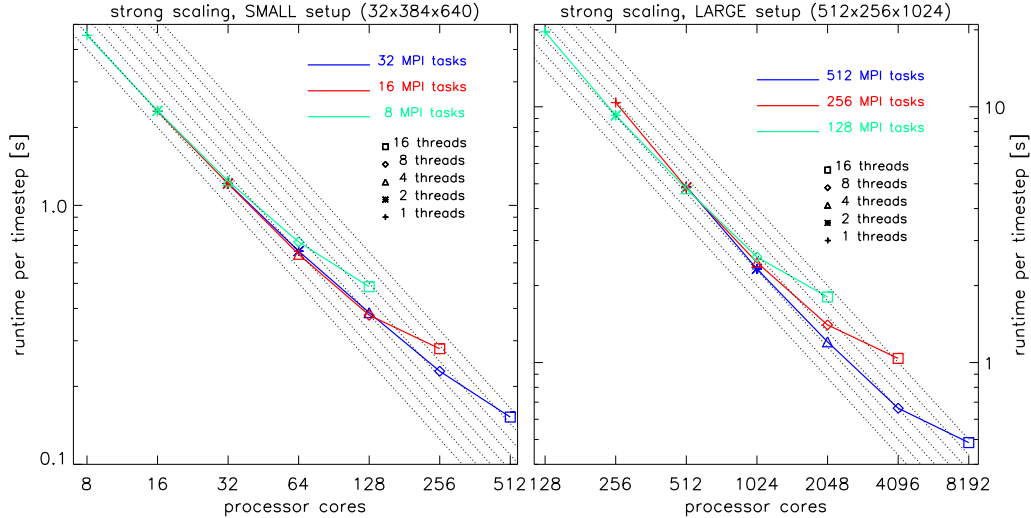


Figure 10: Runtime per time step for the SMALL setup (left panel) and for the LARGE setup (right panel) as a function of the number of cores, $N_{\text{cores}} = N_{\text{tasks}} \cdot N_{\text{threads}}$. Different colors and symbols are used to distinguish runs with different numbers of MPI tasks (N_{tasks}) and OpenMP threads (N_{threads}), respectively. The slope of an ideal scaling curve is indicated by dotted lines.

plain MPI-parallelization using the maximum number of tasks ($N_{\text{tasks}} = n_r$) for the given setup, is assigned an efficiency of 1.0, by definition.

For the SMALL setup (the upper part of Table 1) we observe perfect OpenMP efficiency up to 8 threads (which are pinned to the 8 physical cores of single CPU socket) per MPI-task for the pressure and velocity predictor steps, the corrector step, and also the matrix-vector multiplication in the nonlinear part. When using all 16 cores of a shared-memory node with a single MPI task one notices a slight degradation in OpenMP efficiency due to memory-bandwidth limitations and NUMA effects. The overall parallel efficiency (the bottom row) can be considered as very good up to 128 cores, but gets increasingly bounded by the global transposition (MPI_Alltoall communication) and the limited parallelism in the nonlinear part.

For the LARGE setup (the lower part of Table 1), where the highly scalable linear parts and the matrix-vector multiplication still contribute more than 60% to the total runtime on 4096 processor cores, the code maintains an excellent parallel efficiency of 92%. Even up to 8192 cores an acceptable parallel efficiency of more than 60% is achieved, decreasing the computing time per time step to 0.5s. Using an even larger setup of

SMALL setup (32, 384, 640)										
cores (N_{threads})	32(1)		64(2)		128(4)		256(8)		512(16)	
	T_1 [s]	η	T_2 [s]	η	T_4 [s]	η	T_8 [s]	η	T_{16} [s]	η
nonlinear (1)	0.760	100%	0.435	87%	0.265	72%	0.161	59%	0.105	45%
p prediction (2)	0.084	100%	0.042	99%	0.021	100%	0.011	97%	0.006	84%
\mathbf{u} prediction (3)	0.218	100%	0.109	99%	0.055	98%	0.028	96%	0.016	83%
correction (4)	0.089	100%	0.044	101%	0.022	101%	0.011	99%	0.006	90%
complete step	1.217	100%	0.666	91%	0.385	79%	0.229	66%	0.152	50%
LARGE setup (512, 256, 1024)										
cores (N_{threads})	512(1)		1024(2)		2048(4)		4096(8)		8192(16)	
	T_1 [s]	η	T_2 [s]	η	T_4 [s]	η	T_8 [s]	η	T_{16} [s]	η
nonlinear (1)	1.20	100%	0.67	90%	0.33	91%	0.20	75%	0.19	39%
p prediction (2)	1.12	100%	0.49	114%	0.25	112%	0.13	108%	0.08	88%
\mathbf{u} prediction (3)	1.38	100%	0.61	113%	0.31	111%	0.17	101%	0.11	78%
correction (4)	1.12	100%	0.52	108%	0.28	100%	0.15	93%	0.09	78%
complete step	4.88	100%	2.32	106%	1.20	102%	0.66	92%	0.49	62%

Table 1: Runtime per time step, T_n and parallel efficiency η of the OpenMP parallelization as a function of the number N_{threads} of OpenMP threads per MPI task, using the maximum number of 32 MPI tasks for the SMALL setup, and 512 MPI tasks for the LARGE setup, respectively. Parallel efficiency is conventionally defined as $\eta := T_1/(n \cdot T_n)$ with $n = N_{\text{threads}}$. Different rows show the contributions of the individual algorithmic steps (numbering in brackets chosen according to Section 3.2) to the total runtime of a complete time step (the bottom row).

$(n_r, n_\theta, n_z) = (1792, 384, 512)$, scalability was demonstrated up to 1792 nodes (35 840 Intel Xeon E5-2680 v2 "Ivy Bridge" cores) of the HPC system "Hydra" of the Max-Planck-Society, resulting in a run time of 1s per time step. Computing times of this order enable us to perform highly resolved simulations (*e.g.* of Keplerian flows which require on the order of a million time steps) within a couple of days.

7. Conclusion

With the motivation of exploring high-Reynolds-number turbulent flows, we have developed a highly efficient parallel DNS code for Taylor-Couette flows. The incompressible Navier-Stokes equations in cylindrical coordinates are solved in primitive variables by using an improved projection method proposed by Hugues *et. al.* [24], which is second-order accurate in both

pressure and velocity. This method leads at each time step to the solution of five linear differential equations, either of Poisson or of Helmholtz type, which simplifies significantly the programming of the code. For the spatial discretization, we use a combination of Fourier spectral in axial and azimuthal directions and finite differences in the radial direction, which allow the use of tailored stretched grids. The computing cost scales linearly with the number of grid points in each direction.

In order to reach higher Reynolds numbers and to take full advantage of the modern HPC facilities, the code is parallelized by a hybrid MPI-OpenMP strategy, combining the simplicity of a MPI-based one-dimensional “slab” domain decomposition in Fourier space with efficient exploitation of the remaining coarse-grained parallelism by OpenMP threading. Compared to a flat MPI-parallelization, the hybrid code maps more naturally to the current multi-node, multi-core architectures and, most importantly, reduces inter-node communications, which improves the overall efficiency and scalability. The strong scaling study which was performed with scientifically relevant setups shows a very good scalability of the code up to $\mathcal{O}(10^4)$ cores. This allows to perform simulations with much higher resolutions than previously possible. With the current HPC technology, this code pushes the achievable Re to the order of magnitude of $\mathcal{O}(10^5)$ in DNS of Taylor-Couette flow, which therefore opens up the possibility to study quasi-Keplerian flows at experimentally relevant parameters.

The new code has been shown to be very accurate in various regimes: laminar Couette flow, wavy vortices, transitional and turbulent flow at high Re . With the high efficiency of the hybrid parallel scheme, this code possesses great potential to explore the turbulent TCf in a much broader parameter space.

Acknowledgments

We thank Florian Merz (IBM) for optimizing the global transposition routine. L. Shi and B. Hof acknowledge research funding by Deutsche Forschungsgemeinschaft (DFG) under Grant No. SFB963/1 (project A8). Computations were performed on the HPC system “Hydra” of the Max-Planck-Society at RZG.

References

- [1] L. Rayleigh, On the dynamics of revolving fluids, Proc. R. Soc. Lond. A 93 (1917) 148–154.
- [2] S. Balbus, A turbulent matter, Nature 470 (2011) 475–476.
- [3] H. Ji, M. Burin, E. Scharfman, J. Goodman, Hydrodynamic turbulence cannot transport angular momentum effectively in astrophysical disks, Nature 444 (2006) 343–346.
- [4] E. Scharfman, H. Ji, M. Burin, J. Goodman, Stability of quasi-Keplerian shear flow in a laboratory experiment, Astron. Astrophys. 543 (2012) A94.
- [5] M. S. Paoletti, D. P. Lathrop, Angular momentum transport in turbulent flow between independently rotating cylinders, Phys. Rev. Lett. 106 (2011) 024501.
- [6] M. S. Paoletti, D. P. M. van Gils, B. Dubrulle, C. Sun, D. Lohse, D. P. Lathrop, Angular momentum transport and turbulence in laboratory models of Keplerian flows, Astron. Astrophys. 547 (2012) A64.
- [7] M. Avila, Stability and angular-momentum transport of fluid flows between corotating cylinders, Phys. Rev. Lett. 108 (2012) 124501.
- [8] S. B. Pope, Turbulent Flows, Cambridge University Press, 2000.
- [9] S. A. Orszag, G. S. Patterson, Numerical simulation of three-dimensional homogeneous isotropic turbulence, Phys. Rev. Lett. 28 (1972) 76–79.
- [10] P. Moin, K. Mahesh, Direct numerical simulations: A tool in turbulence research, Ann. Rev. Fluid Mech. 30 (1998) 539–578.
- [11] J. Jiménez, Computing high-Reynolds-number turbulence: will simulations ever replace experiments?, J. of Turbulence 4 (2003) 1–13.
- [12] P. Spalart, Direct simulation of a turbulent boundary layer up to $Re_\theta = 1410$, J. Fluid Mech. 187 (1988) 61–98.

- [13] P. Schlatter, R. Örlü, Assessment of direct numerical simulation data of turbulent boundary layers, *J. Fluid Mech.* 659 (2010) 116–126.
- [14] J. Kim, P. Moin, R. Moser, Turbulence statistics in fully developed channel flow at low Reynolds number, *J. Fluid Mech.* 177 (1987) 133–166.
- [15] S. Hoyas, J. Jiménez, Scaling of the velocity fluctuations in turbulent channels up to $Re_\tau = 2003$, *Phys. Fluids* 18 (2006) 011702.
- [16] J. Eggels, F. Unger, M. Weiss, J. Westerweel, R. Adrian, R. Friedrich, F. Nieuwstadt, Fully developed turbulent pipe flow: a comparison between direct numerical simulation and experiment, *J. Fluid Mech.* 268 (1994) 175–209.
- [17] X. Wu, J. Baltzer, R. Andrian, Direct numerical simulation of a 30R long turbulent pipe flow at $R^+ = 685$: large- and very large-scale motions, *J. Fluid Mech.* 698 (2012) 235–281.
- [18] K. Coughlin, P. S. Marcus, Turbulent bursts in Couette-Taylor flow, *Phys. Rev. Lett.* 77(11) (1996) 2214–2217.
- [19] H. Brauckmann, B. Eckhardt, Direct numerical simulation of local and global torque in Taylor-Couette flow up to $Re = 30000$, *J. Fluid Mech.* 718 (2013) 398–427.
- [20] R. D. Moser, P. Moin, A. Leonard, A spectral numerical method for the Navier-Stokes equations with applications to Taylor-Couette flow, *J. Comput. Phys.* 52 (1983) 524–544.
- [21] A. Meseguer, M. Avila, F. Mellibovsky, F. Marques, Solenoidal spectral formulations for the computation of secondary flows in cylindrical and annular geometries, *Eur. Phys. J.* 146 (2007) 249–259.
- [22] P. S. Marcus, Simulation of Taylor-Couette flow. Part 1. numerical methods and comparison with experiment, *J. Fluid Mech.* 146 (1984) 45–64.
- [23] D. Kasloff, H. Tal-Ezer, A modified Chebyshev pseudospectral method with an $\mathcal{O}(N^{-1})$ time step restriction, *J. Comput. Phys.* 104 (1993) 457–469.

- [24] S. Hugues, A. Randriamampianina, An improved projection scheme applied to pseudospectral methods for the incompressible Navier-Stokes equations, *Int. J. Numer. Meth. Fluids* 28 (1998) 501–521.
- [25] P. Gresho, R. L. Sani, On pressure boundary conditions for the incompressible Navier-Stokes equations, *Int. J. Numer. Methods Fluids* 7 (1987) 1111–1145.
- [26] S. A. Orszag, A. T. Patera, Secondary instability of wall-bounded shear flows, *J. Fluid Mech.* 128 (1983) 347–385.
- [27] B. Fornberg, A practical guide to pseudospectral methods, Cambridge university press, 1998.
- [28] G. E. Karniadakis, M. Israeli, S. A. Orszag, High-order splitting methods for the incompressible Navier-Stokes equations, *J. Comput. Phys.* 97 (1991) 414–443.
- [29] J. Dongarra, P. Beckman, et al., The international exascale software roadmap, *International Journal of High Performance Computer Applications* 25 (2011). ISSN 1094-3420.
- [30] M. Frigo, S. G. Johnson, The design and implementation of FFTW3, *Proceedings of the IEEE* 93 (2005) 216–231. Special issue on “Program Generation, Optimization, and Platform Adaptation”.
- [31] G. P. King, Y. Li, W. Lee, H. L. Swinney, P. S. Marcus, Wave speeds in wavy Taylor-vortex flow, *J. Fluid Mech.* 141 (1984) 365–390.
- [32] R. P. Brent, *Algorithms for Minimization without Derivatives*, Dover Publications, 2002.
- [33] L. Shi, M. Avila, B. Hof, Scale invariance at the onset of turbulence in Couette flow, *Phys. Rev. Lett.* 110 (2013) 204502.
- [34] S. Marezke, B. Hof, M. Avila, Transient growth in linearly stable Taylor-Couette flows, *arXiv:1304.7032* (2013).